Scanning Near-Field Millimeter-Wave Microscopy Using a Metal Slit as a Scanning Probe

Tatsuo Nozokido, *Member, IEEE*, Jongsuck Bae, *Senior Member, IEEE*, and Koji Mizuno, *Fellow, IEEE*

***Abstract*—In this paper, a novel type of scanning near-field millimeter-wave microscopy using a metal slit-type probe is proposed. A tapered reduced-height rectangular waveguide forms the slit aperture, which has a width much smaller than one wavelength λ and length of the order of λ. The slit probe can be operated in the TE_{10} mode and, thus, results in high transmission efficiency, even when the width is exceedingly small. An image reconstruction algorithm based on computerized tomographic imaging is used to obtain two-dimensional near-field images. Experiments performed at 60 GHz ($\lambda = 5$ mm) show that image resolution equal to the slit width ($\sim$80 μm) is achieved. As an application of this scanning slit microscopy, visualization of transition phenomena of photoexcited free carriers in a silicon have been successfully demonstrated, yielding useful information on the dynamics of free carriers in semiconductor materials.**

***Index Terms*—Free carriers, millimeter-wave, scanning near-field microscopy, slit-type probe, visualization.**

I. INTRODUCTION

SINCE scanning near-field microscopy was first demonstrated at microwave frequencies by Ash and Nicholls with a resolution of $\sim\lambda/60$ [1], near-field imaging has been accomplished in a variety of instruments, which cover frequencies spanning the microwave to optical regions. Thus far, many kinds of near-field probes have been proposed and used because they determine the image resolution and sensitivity attainable in scanning near-field microscopy. In the optical region, metal-coated tapered optical fibers with a submicroscopic aperture at the apex have been generally utilized as scanning probes [2]–[4]. Since the aperture diameter of the fiber probes should be much less than the observation wavelength to achieve subwavelength resolution, the probes are usually operated below the cutoff frequency [4], thus resulting in low transmission efficiency [5]. In the microwave and millimeter-wave regions, the diversity of probes is bigger than in the optical region. The coaxial probe [6]–[10] is made up of a fine coaxial cable with a sharpened central conductor protruding from the outer shielding. The sharp tip is a wide-band probe, which does not suffer from the cutoff effect. The probe is usually operated in conjunction with a resonant structure to increase sensitivity, although this combination sacrifices the probe's wide-band nature. Its spatial resolution is determined by the tip size of the inner conductor. A small aperture in the conducting screen [1] and an aperture at the apex of a tapered circular waveguide [7], [11] are utilized for scanning near-field microscopy. For the same reason as in the optical probe, the structure leads to diminished sensitivity. Their spatial resolutions are determined by the size of the aperture. A miniature loop is used as a scanning probe in conjunction with a microstrip resonator [12].

The slit-type probe was first proposed by Kawata *et al.* in 1995 [13]. The probe has a metal slit aperture, which has a width much smaller than one wavelength λ and length of the order of λ. The slit probe can be operated in the TE_{10} mode and, thus, results in high transmission efficiency because of no cutoff effect. They used a narrow metal slit aperture fabricated on a ZnSe lens for infrared spectroscopy. Another type of the slit probe is a narrow resonant slit fabricated at the end of a rectangular waveguide proposed by Golosovsky *et al.* [14]. The transmission efficiency of the resonant slit probe can be nearly unity by selecting precisely the slit dimension. Since the width of the slit-type probe is much smaller than λ, while the length of the slit is on the order of λ, by simply raster scanning the probe to obtain two-dimensional near-field images, image resolution along the slit width can be much smaller than λ, while unfortunately, the resolution along the slit length is of the order of λ [13], [14].

In this paper, we propose a new type of scanning near-field millimeter-wave microscopy using a metal slit at the end of a tapered rectangular waveguide as a scanning probe, and an image reconstruction algorithm based on computerized tomographic (CT) imaging to reconstruct two-dimensional near-field images with subwavelength resolutions for all directions. Our probe can be operated over a much wider bandwidth than the resonant slit probe [14] described above because of its operation without resonance. Hence, the probe is suitable for high-speed imaging. To demonstrate this, as an application of this microscopy technique, we show experimental results for the visualization of transition phenomena of photoexcited free carriers in a silicon substrate.

II. EXPERIMENTAL

Fig. 1 is a schematic drawing of our scanning near-field millimeter-wave microscope, and shows the slit-type probe used. A tapered reduced-height waveguide forms the slit aperture. The wide dimension of the slit and that of the WR-19 waveguide are identical, but the waveguide height is tapered down to 80 μm ($\lambda/60$). The frequency used in our experiments was 60 GHz ($\lambda = 5$ mm). The slit probe and a receiving horn were both mounted on fixed stages and connected to a WILTRON 360B

Manuscript received November 4, 1999.

T. Nozokido was with the Photodynamics Research Center, The Institute of Physical and Chemical Research (RIKEN), Sendai 980-0868, Japan. He is now with the Research Institute of Electrical Communication, Tohoku University, Sendai 980-8577, Japan (e-mail: nozokido@riec.tohoku.ac.jp).

J. Bae and K. Mizuno are with the Research Institute of Electrical Communication, Tohoku University, 2-1-1 Katahira, Sendai 980-8577, Japan.

Publisher Item Identifier S 0018-9480(01)01684-2.

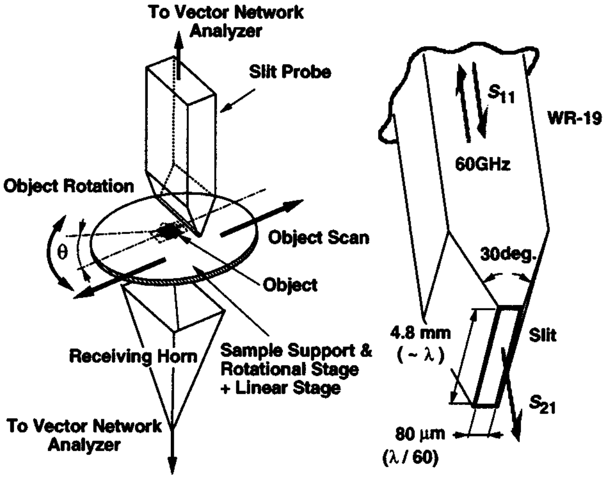

(a) (b)

Fig. 1. (a) Experimental setup for scanning near-field millimeter-wave microscopy using a tapered rectangular waveguide probe with a slit aperture. (b) Dimensions of the probe. λ is the wavelength in free space.

vector network analyzer (VNA) via waveguide-to-coaxial transformers. The object to be imaged was mounted onto the scanner, which consists of rotational and linear stages driven by stepping motors, and was moved under the probe at a constant separation of 2 ~200 μm. The VNA and scanner were controlled by a computer. The object was scanned linearly for different object-rotation angles θ. This scan method is quite different from the raster scanning technique used in other conventional scanning near-field microscopes. The 60-GHz millimeter-wave radiation was fed to the probe. The reflected signal from the probe S_{11} and the signal received by the horn antenna S_{21} were obtained in reflection and/or transmission modes through the VNA, and were then processed into images by the filtered back-projection (FBP) method [15], which is the most commonly used image reconstruction method in CT imaging. The details of the image reconstruction are described in the following section.

In the experiments, the object was scanned while the slit probe remained fixed. This method of data acquisition can be clearly described if the object is fixed and the slit probe is scanned as shown in Fig. 2. In this figure, each arrow indicates the direction of the slit length. The signal from the probe reflects the integral of the near fields along the slit length so that the data acquired during a linear scan is a projection of the near-field distribution on the "A"-shaped object toward the direction indicated by the arrows. Since each projection data set contains all the pixel information in the field of view, our microscope is suitable for obtaining the outline of an image using fewer data points than in the case of a conventional point-type probe, which should be raster scanned.

III. THEORY OF TWO-DIMENSIONAL IMAGE RECONSTRUCTION

We are using an image reconstruction algorithm based on CT imaging to reconstruct two-dimensional near-field images. The data acquired through the scans depicted in Fig. 2 are processed by the FBP method. Although the method is well-known in computerized tomography [15]–[17], in the following, we will show the essence of the method, being related with the near-field data acquisition.

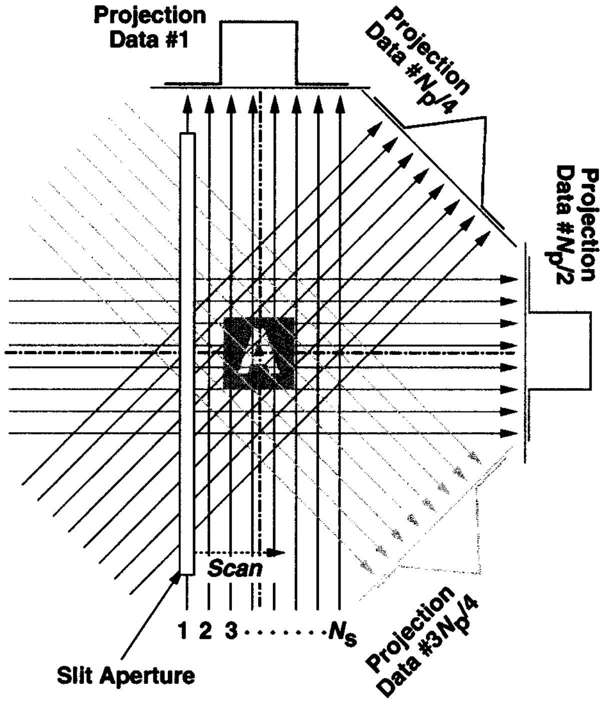

Fig. 2. Scan method in the case where the object is fixed and the slit probe is scanned. In this figure, N_p shows the total number of projections and N_s is the number of sampling points for the linear scan.

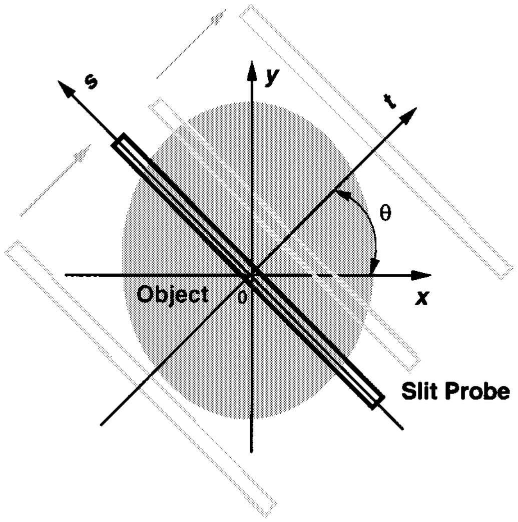

Fig. 3. Coordinate systems used to describe the data acquisition process. The $(t,\, s)$ coordinate system is a rotated version of the original $(x,\, y)$ system by an angle of θ.

We will use the rectangular coordinate systems defined in Fig. 3 to describe the data-acquisition process. The slit probe is linearly scanned in parallel with the s-axis, where the center of the slit aperture always coincides with the t-axis. The signal from the probe or the horn antenna $P_\theta(t)$ as a function of t and θ can be expressed as

$$P_\theta(t) \propto \int E_{\text{illum}}(t,\, s) \cdot f(t,\, s) \cdot E_{\text{collect}}(t,\, s)\, ds \qquad (1)$$

where $E_{\text{illum}}(t, s)$ is an illuminating field, $f(t, s)$ is the object function that represents intrinsic electromagnetic properties of the object, and $E_{\text{collect}}(t, s)$ represents sensitivity distribution of the probe or the horn antenna in signal reception [18]. $P_\theta(t)$, $E_{\text{illum}}(t, s)$, $f(t, s)$, and $E_{\text{collect}}(t, s)$ are the complex valued quantities. The vector product $E_{\text{illum}}(t, s) \cdot f(t, s)$ defines the reflected field $E_r(t, s)$ and the transmitted field $E_t(t, s)$ from the object. These fields, i.e., $E_r(t, s)$ and $E_t(t, s)$, are determined by the near-field spatial distribution on the object and form the image of the object with subwavelength resolutions for all directions through the FBP method described below.

If the illuminating field $E_{\text{illum}}(t, s)$ and the sensitivity distribution $E_{\text{collect}}(t, s)$ are assumed to be uniform, $P_\theta(t)$ can be written as

$$P_\theta(t) \propto \int f(t, s)\, ds. \tag{2}$$

This equation means that the signals from the probe and horn antenna reflect the integral of the object function along the slit length s. Suppose that the Fourier transform of the object function $f(t, s)$ is indicated by $F(u, v)$, $f(x, y)$ can be expressed as

$$f(x, y) = \int_{-\infty}^{\infty} \int_{-\infty}^{\infty} F(u, v) e^{j2\pi(ux+vy)} dx\, dy. \tag{3}$$

Exchanging the rectangular coordinate system in the frequency domain (u, v) for a polar coordinate system (w, θ), we can write the inverse Fourier transform of a polar function as

$$f(x, y) = \int_0^{2\pi} \int_0^{\infty} F(w, \theta) e^{j2\pi(x \cos\theta + y\, \sin\theta)} w\, dw\, d\theta. \tag{4}$$

By splitting the integral into two by considering θ from 0 to π and from π to 2π, and by using the property

$$F(w, \theta + \pi) = F(-w, \theta) \tag{5}$$

the above expression for $f(x, y)$ can be written as

$$f(x, y) = \int_0^{\pi} \left[\int_{-\infty}^{\infty} F(w, \theta) |w| e^{j2\pi wt}\, dw \right] d\theta \tag{6}$$

where t is expressed as

$$t = x\cos\theta + y\sin\theta. \tag{7}$$

$P_\theta(t)$ is a projection data, which can be measured. According to the Fourier slice theorem [15], the Fourier transform of the projection data $S_\theta(w)$ is related to the Fourier transform of the object function $F(w, \theta)$ as follows:

$$F(w, \theta) = S_\theta(w) = \int_{-\infty}^{\infty} P_\theta(t) e^{-j2\pi wt}\, dt. \tag{8}$$

By making use of (8), the final form for $f(x, y)$ results in

$$\begin{aligned} f(x, y) &= \int_0^{\pi} Q_\theta(x\cos\theta + y\sin\theta)\, d\theta \\ &= \int_0^{\pi} Q_\theta(t)\, d\theta \end{aligned} \tag{9}$$

where $Q_\theta(t)$ is the filtered projection data expressed as

$$Q_\theta(t) = \int_{-\infty}^{\infty} S_\theta(w) |w| e^{j2\pi wt}\, dw. \tag{10}$$

Reconstruction of near-field images can be performed using the above two equations. The flow of data processing for the images is as follows.

Step 1) Fourier transforming projection data $P_\theta(t)$ with regard to t to yield $S_\theta(w)$.
Step 2) Multiplying the result $S_\theta(w)$ by the filter function $|w|$.
Step 3) Inverse Fourier transforming the product $S_\theta(w)|w|$.
Step 4) Back projecting the result of the last step $Q_\theta(t)$ to the image plane (x, y).

Steps 1)–4) should be repeated for all θ, and the sum of all the back-projected images provides the reconstructed image. Note that the filtered projection $Q_\theta(t)$ makes the same contribution to the reconstruction at all the points in the image plane (x, y), which correspond to a value of $t = x\cos\theta + y\sin\theta$ for a given value of θ. Computer implementation of the FBP method is the same as in [15].

To discuss the signal detection method needed for two-dimensional near-field image reconstruction, we express the signal P from the probe or the horn antenna in a discrete form in the case with coherent illumination as follows:

$$P \propto \sum_{n=1}^{N} E_n e^{j(\omega t + \theta_n)} \tag{11}$$

where ω and t are the angular frequency and time, respectively. In this equation, the length of the slit is divided into N sections and the near field in each section is expressed in phasor form. The resulting signals $P_{\text{heterodyne}}$ and P_{power} when the heterodyne and the power detections are adopted for P can be expressed as

$$P_{\text{heterodyne}} \propto \sum_{n=1}^{N} E_n e^{j\theta_n} \tag{12}$$

and

$$P_{\text{power}} \propto \sum_{n=1}^{N} |E_n|^2 + 2\sum_{i \neq m} |E_l| \cdot |E_m| \cos(\theta_l - \theta_m) \tag{13}$$

respectively. Equation (12) is an alternative expression for (2), which is the precondition for two-dimensional image reconstruction by the FBP method. The second term in the right- hand side of (13) is a deviation from the precondition and may cause some artifacts in the reconstructed images by the FBP method. Hence, under coherent illumination, heterodyne detection should be utilized for the two-dimensional image reconstruction.

IV. RESULTS

In this section, we demonstrate the two-dimensional near-field image reconstruction using the slit probe and algorithm based on CT imaging. First, measured and calculated reflection coefficients of the probe as a function of frequency are presented to show the wide-band nature of the slit probe, and to give the transmission coefficient of the probe. Next, one-dimensional scans of a test sample are presented in order to show the validity of the precondition for the two-dimensional near-field

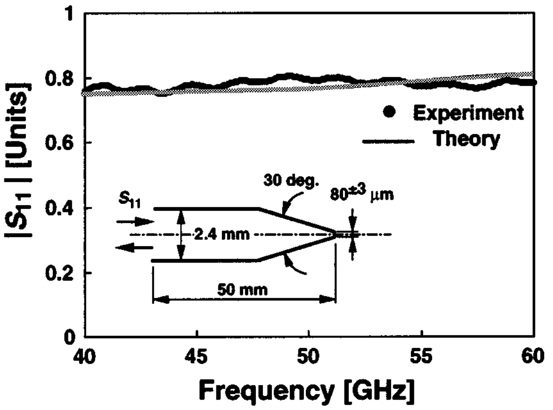

Fig. 4. Comparison of measured and calculated results of the amplitude of the reflection coefficient $|S_{11}|$ as a function of frequency. The cross section of the probe is depicted in the inset. The slit width has a variation of ±3 mm from the average value of 80 μm. In the experiment, the probe was directed to free space.

image reconstruction by the FBP method. Near-field images obtained in the experiment are presented and their resolutions are evaluated. We compare two near-field images, one of which is reconstructed with heterodyne detection, the other with power detection. Finally, we show the application of our microscope for the visualization of transition phenomena of photoexcited free carriers in a silicon substrate.

A. Probe Characteristic

In order to estimate the transmission coefficient of the slit probe, we measured the reflection coefficient S_{11} of the probe and compared it with the calculated value using an equivalent-circuit model. Fig. 4 shows the results, where the measured and calculated results of the amplitude of the reflection coefficient $|S_{11}|$ are plotted as a function of frequency. The cross section of the probe is depicted in the inset of this figure. The tapered section of the probe can be assumed to be a series connection of several waveguides with different heights. The impedances and propagation constants of these waveguides in the TE_{10} operation were calculated, and an equivalent-circuit model for the probe was derived. In the calculation, the slit probe is assumed to be terminated by the lumped impedance of free space Z_0 and the propagation loss constants are calculated using the ten times larger value of the dc resistivity of gold, with which the probe is coated. Fig. 4 shows that the measured and calculated results agree well. From the calculation, the power transmission coefficient at 60 GHz is estimated as 20%. In the metal-coated tapered optical fiber probes with aperture diameters of less than $\lambda/10$, the transmission coefficient has been reported as 10^{-5}% or less [5], which is $\sim 10^5$ times smaller in value than the estimated value of the slit probe, which is free from the cutoff effect.

B. Validity of the Precondition for Two-Dimensional Near-Field Image Reconstruction

In order to reconstruct images correctly using the FBP method, the illuminating field E_{illum} and the sensitivity distribution E_{collect} should be uniform, as described in Section III. To check this for our slit probe, reflection coefficient S_{11} was measured using metal lines with different lengths as an object.

Fig. 5 shows one-dimensional scans of metal lines deposited onto a quartz plate. The lengths of the lines vary from 0.2 to 2.0 mm, while the widths of the lines are all the same. The object was linearly scanned over 6400 μm with a step size of 16 μm. Probe-to-object separation was kept at a constant value of 10 μm. The measured reflection coefficient S_{11} was processed in order to set the measured data for the quartz plate as $|S_{11}| = 0$ and $\arg(S_{11}) = 0$. This was done by subtracting the reflection coefficient corresponding to the quartz plate from each of the measured data in vectorial operation. The resulting differences in amplitude and phase are shown in Fig. 5(b) and (c), respectively. If the amplitude is proportional to the length of the metal lines, and the phase remains constant regardless of the length of the metal lines, then the validity of the precondition for two-dimensional image reconstruction can be proven. This holds true for the phase difference $\Delta \arg(S_{11})$ in Fig. 5(c). In

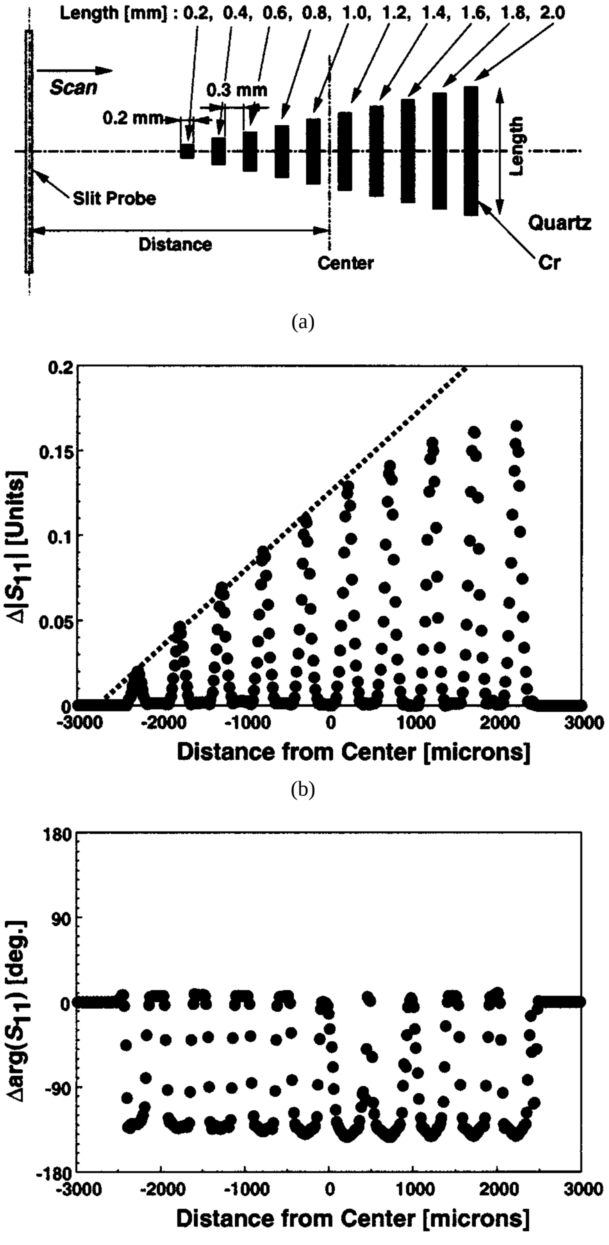

(a)

(b)

(c)

Fig. 5. One-dimensional scans of metal lines deposited onto a quartz plate. (a) Object configuration. (b) Amplitude variation of reflection coefficient. (c) Phase variation of reflection coefficient.

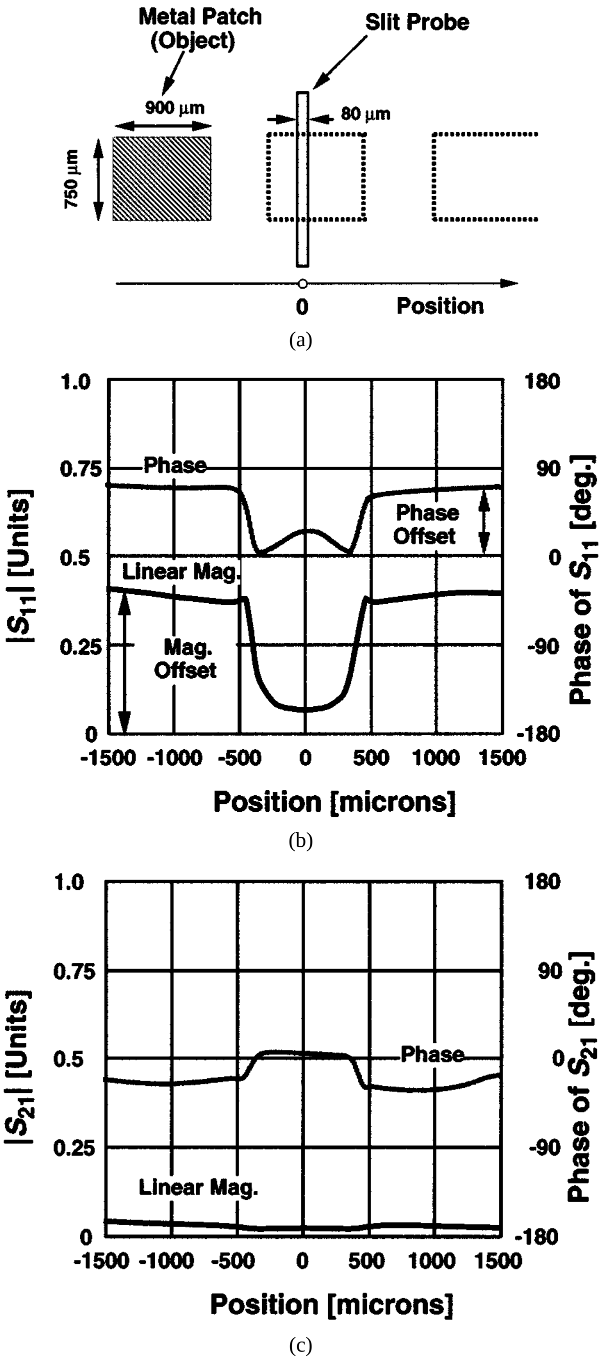

(a)

(b)

(c)

Fig. 6. One-dimensional scans of a metal patch. (a) Situation of the scan. (b) Amplitude and phase variations in reflection mode. (c) Amplitude and phase variations in transmission mode.

the case of the amplitude difference, $\Delta|S_{11}|$ in Fig. 5(b), where the dotted line indicates the ideal variation, deviations from the dotted line arise when the metal lines with lengths longer than 1.2 mm were observed by the slit probe. This implies that the size of the object under observation should be less than 1.2 mm × 1.2 mm for perfect reconstruction. The effect of this deviation onto images, and the method for eliminating the effect, will be discussed again in detail in Section V.

C. Reconstructed Near-Field Images

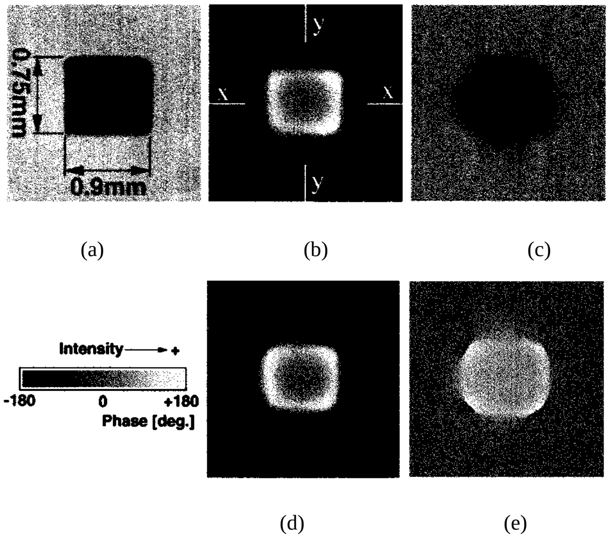

(a) (b) (c)

(d) (e)

Fig. 7. Reconstructed images of a metal patch. (a) Optical image. (b) Intensity image in reflection mode. (c) Phase image in reflection mode. (d) Intensity image in transmission mode. (e) Phase image in transmission mode.

TABLE I
EXPERIMENTAL CONDITIONS

Image size	: 2100 μm × 2100 μm
Sampling interval for linear scan	: 40 μm
Sampling points for linear scan	: 74 pt.
Sampling interval for rotational scan	: 2.43 deg.
Total number of projections	: 74
Probe-to-object separation	: 10 μm

Fig. 6 shows measured projection data in reflection mode S_{11} signals in linear magnitude and phase, and measured data in transmission mode S_{21} signals obtained by linearly scanning the object. The object was a 0.9 mm × 0.75 mm metal patch supported by a quartz plate with a thickness of 1.87 mm. Before processing these projection data by the FBP method, e.g., in the reflection mode, the vector, which consists of the magnitude and phase offsets depicted in Fig. 6(b), has to be subtracted from all the data. This operation should be done in order to prevent aliasing artifacts [15], which occur due to data truncation in the case without the operation. The effect of this operation on the reconstructed images is that the image intensities corresponding to the quartz plate in the intensity and phase images are set to zero. Since the projection data have intensity and phase information, after image reconstruction, intensity and phase images are obtained for each mode of the measurements.

The reconstructed images are shown in Fig. 7. They were obtained under the experimental conditions listed in Table I. Since the highest resolution achievable was expected to be of the order of the width of the slit probe, we set the sampling interval for the linear scan as half of the slit width, according to the sampling theorem [19]. For a well-balanced reconstructed image, the total number of projections is set equal to the number of sampling points for the linear scan [15].

We tried to estimate the resolution of the intensity image in reflection mode shown in Fig. 7(b). Fig. 8(a) shows one-dimensional intensity profiles along the line x–x and y–y in Fig. 7(b). By differentiating the rising parts in the profiles indicated by an asterisk, line spread functions (LSFs) [19] can be calculated and are shown in Fig. 8(b) and (c). Note that the full widths

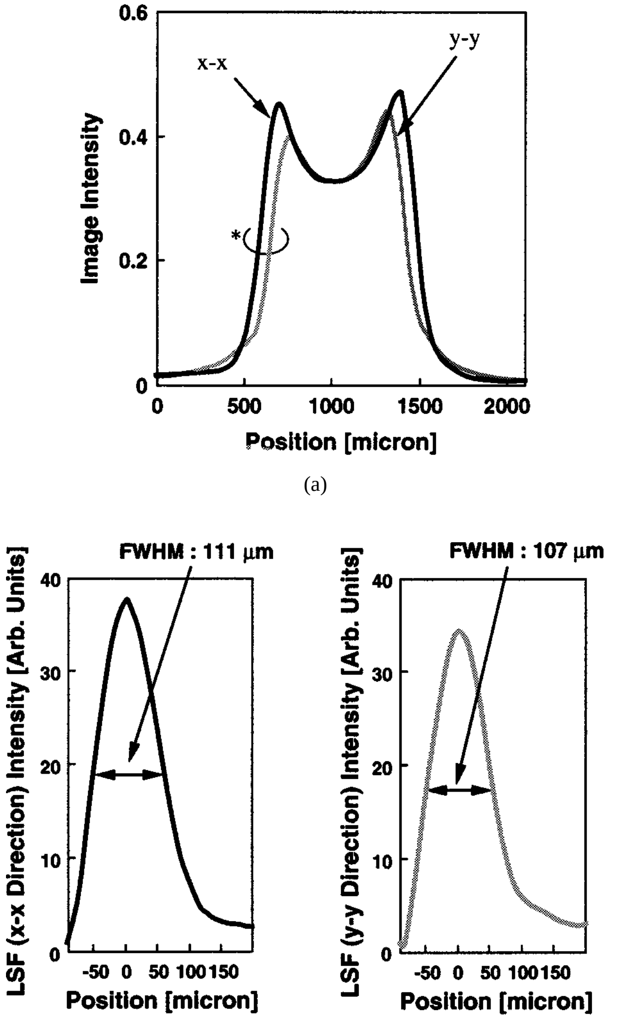

(a)

(b) (c)

Fig. 8. Evaluation of image resolution: (a) one-dimensional intensity profiles along the line $x - x$ and $y - y$ in Fig. 7(b) and (b), (c) LSFs.

at half maximum FWHMs of these LSFs are almost the same. By averaging the FWHMs, we determine the image resolution as 110 μm, which is nearly equal to the width of the slit probe used.

Probe-to-object separation is the most significant factor in determining image resolution and intensity because the evanescent field, which can provide subwavelength resolution in the near-field region of a scanning probe, dies off exponentially away from the probe surface [20]. Fig. 9 shows intensity images in the reflection mode when the probe-to-object separation was varied. The object and experimental conditions are the same as those mentioned above. As the probe-to-object separation gets larger, the image intensity is getting lower and the image itself vanishes. Using the images in Fig. 9, image resolution as a function of separation can be estimated with LSFs and is plotted in Fig. 10. The result in Fig. 10 shows that as the object is separated from the probe, the image resolution gets worse, and the finest resolution achievable is equal to the width of the slit probe used. Finer samplings and/or more projections did not provide any improvements in the image resolution in Fig. 10.

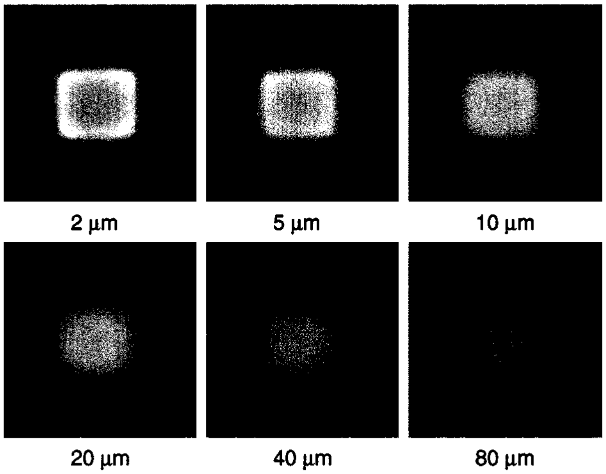

Fig. 9. Intensity images in the reflection mode when the probe-to-object separation was varied. The separation is indicated under each image.

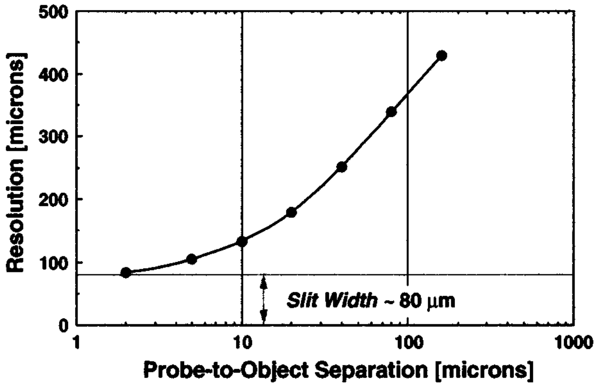

Fig. 10. Image resolution as a function of probe-to-object separation.

D. Comparison of Images Obtained with Heterodyne and Power Detection

In Section III, we note that, in the case with coherent illumination, the signal from the probe should be detected with heterodyne detection in order to reconstruct two-dimensional near-field images. Measured raw data, which is a set of several projection data, can easily be converted into the raw data obtained with power detection. Since the measured data is obtained with heterodyne detection via the VNA and is complex valued, the squared amplitude of the data is equivalent to the raw data obtained with power detection. Measured raw data of metal patches deposited onto a quartz plate was converted to the equivalent raw data. These two data sets were reconstructed into intensity images. Fig. 11 compares images of the metal patches. The image in Fig. 11(b), which is an intensity image reconstructed with heterodyne detection, reflects well the structure of the object, while it is obvious that artifacts arise in Fig. 11(c), which is an intensity image reconstructed with power detection. This is proof that under coherent illumination, heterodyne detection should be utilized for two-dimensional image reconstruction. Under incoherent illumination, power detection can be applied to the image reconstruction without artifacts because the second term in the right-hand side of (13) tends to zero.

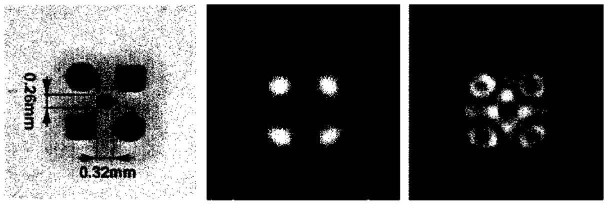

(a) (b) (c)

Fig. 11. Comparison of images of metal patches. (a) Optical image. (b) Reconstructed intensity image with heterodyne detection. (c) With power detection. The raw data was measured in reflection mode.

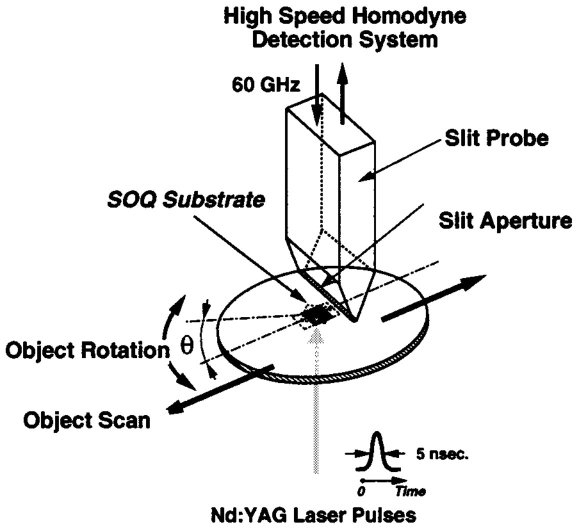

Fig. 12. Experimental scheme for visualizing transition phenomena of photoexcited free carriers in reflection mode.

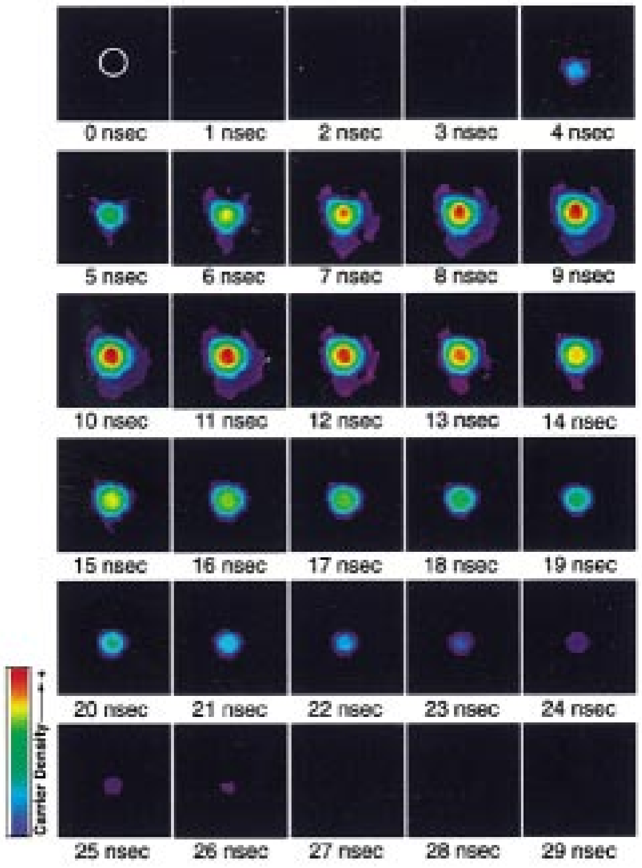

Fig. 13. Temporal evolution of photoexcited free-carrier distribution. The time under each image indicates the time after the photo excitation began. The circle in the image at 0 ns shows the photoexcited region.

E. Application

The benefit of using microwaves and millimeter waves in scanning near-field microscopy lies in the promise of new types of material contrast. A good example is the mapping of electronic transport properties. We have succeeded in visualizing photoexcited free-carrier distribution in the steady-state condition in a silicon substrate using millimeter-wave microscopy [21]. As demonstrated in Section IV-A, the tapered slit probe is suitable for measuring high-speed phenomena in objects because of its wide-band characteristic. Here, we demonstrate the application of our microscope for the visualization of transition phenomena of photoexcited free carriers in a silicon substrate, i.e., time-resolved imaging of photoexcited free carriers. A high-speed homodyne detection system with a response time of 0.4 ns was constructed. The experimental setup is shown in Fig. 12. The object was a silicon on quartz (SOQ) substrate.[1] The thicknesses of the silicon and quartz layers were 0.2 μm and 1.2 mm, respectively. Optical pulses from a Q-switched Nd : YAG laser passing through the quartz layer generated free carriers in the silicon layer. The Nd : YAG wavelength was 355 nm, the repetition rate was 10 Hz, the pulsewidth was 5 ns, and the pulse energy was 30 mJ. The photoexcited area was 0.5 mm in diameter. The density of free carriers generated was estimated to be as high as 10^{+17}/cm^3 [22]. During the object scans, the waveforms from the detection system monitored by an oscilloscope were stored against each position of the object. The stored waveforms were then arranged into images, each of which represents a different time phenomenon. Fig. 13 shows the reconstructed images. The image size and the resolution are 1980 μm × 1980 μm and 120 μm, respectively. Free-carrier generation and extinction processes are clearly imaged in these images. The diffusion process of free carriers is also observed, and the images show that the free carriers generated did not diffuse uniformly in the silicon layer. This indicates that the silicon layer has some kind of defect distribution along the surface directions of the SOQ substrate. Animation of the images in Fig. 13 can be seen on our Web site.[2]

V. DISCUSSION

Fig. 5(b) shows that the signal intensity is not proportional to the size of the object under observation. This means that the slit probe has a sensitivity distribution. This sensitivity distribution is due to the fact that the illuminating field $E_{\rm illum}$ and the sensitivity distribution of the probe in signal reception $E_{\rm collect}$ are not uniform along the slit length. These two factors determine the sensitivity distribution of the slit probe in reflection mode. We have done some experiments to measure the sensitivity distribution, i.e., the product of $E_{\rm illum}$ and $E_{\rm collect}$, and

---

[1] Provided by the Shin-Etsu Handotai Company, Ltd., Tokyo, Japan.

[2] [Online]. Available: http://www.mizuno.riec.tohoku.ac.jp/nfmw/nfmw_anime.html

found that the distribution can be approximated by the square of the E-field intensity distribution of the TE_{10} mode [23]. Computer simulation results show that this kind of sensitivity distribution modifies and spoils the low-frequency components of the true image if the FBP method is applied [24]. The FBP method is a transform-based one, assuming that the precondition previously mentioned holds true and, therefore, it is difficult to include the sensitivity distribution in its reconstruction process. To circumvent this problem, a conjugate gradient method [16] might successfully be applied to the image reconstruction. The method is a kind of algebraic reconstruction algorithm based on the matrix representation between an image and measured data and, thus, deals well with this kind of sensitivity distribution in its calculation. We have some preliminary results on correction of image distortion by the conjugate gradient method by taking into account the sensitivity distribution [23].

VI. CONCLUSIONS

A novel type of scanning near-field millimeter-wave microscopy using a metal slit at the end of a tapered rectangular waveguide as a scanning probe and an image reconstruction algorithm based on CT imaging has been proposed and demonstrated in this paper. The data-processing and the signal-detection method needed for two-dimensional near-field image reconstruction have also been described and experimentally verified. Experiments performed at 60 GHz ($\lambda = 5$ mm) show that two-dimensional near-field intensity images can be obtained with a resolution of 82 μm ($\sim\lambda/60$), which is equal to the width of the slit probe used. The slit probe has the advantages of high transmission efficiency and wide frequency bandwidth. To demonstrate this, scanning slit microscopy has been applied to visualize transition phenomena of photoexcited free carriers in a silicon substrate. The images obtained in the experiment have clearly visualized generation, extinction, and diffusion processes of free carriers.

ACKNOWLEDGMENT

The authors wish to thank T. Fujii, Tokohu University, Sendai, Japan, and H. Minamide, Tokohu University, Sendai, Japan, for their experimental assistance, and C. M. Mann, Rutherford Appleton Laboratory, Oxfordshire, U.K., for helpful discussions. The authors are also grateful to T. Abe, Shin-Etsu Handotai Company, Ltd., Tokyo, Japan, for providing the SOQ substrate.

REFERENCES

[1] E. A. Ash and G. Nicholls, "Super-resolution aperture scanning microscope," *Nature*, vol. 237, pp. 510–512, June 1972.

[2] D. W. Pohl, W. Denk, and M. Lanz, "Optical stethoscopy: Image recording with resolution $\lambda/20$," *Appl. Phys. Lett.*, vol. 44, pp. 651–653, Apr. 1984.

[3] E. Betzig and J. K. Trautman, "Near-field optics: Microscopy, spectroscopy, and surface modification beyond the diffraction limit," *Science*, vol. 257, pp. 189–195, July 1992.

[4] E. L. Buckland, P. J Moyer, and M. A. Paesler, "Resolution in collection-mode scanning optical microscopy," *J. Appl. Phys.*, vol. 73, pp. 1018–1028, Feb. 1993.

[5] G. A. Valaskovic, M. Holton, and G. H. Morrison, "Parameter control, characterization, and optimization in the fabrication of optical fiber near-field probes," *Appl. Opt.*, vol. 34, pp. 1215–1228, Mar. 1995.

[6] M. Fee, S. Chu, and T. W. Häsch, "Scanning electromagnetic transmission line microscope with sub-wavelength resolution," *Opt. Commun.*, vol. 69, pp. 219–224, Jan. 1986.

[7] F. Keilmann, "FIR microscopy," *Infrared Phys. Technol.*, vol. 36, pp. 217–224, 1995.

[8] T. Wei, X.-D. Xiang, W. G. Wallace-Freedman, and P. G. Schultz, "Scanning tip microwave near-field microscope," *Appl. Phys. Lett.*, vol. 68, pp. 3506–3508, June 1996.

[9] F. Keilmann, D. W. van der Weide, T. Eickelkamp, R. Merz, and D. Stökle, "Extreme sub-wavelength resolution with a scanning radio-frequency transmission microscope," *Opt. Commun.*, vol. 129, pp. 15–18, Aug. 1996.

[10] C. P. Vlahacos, R. C. Black, S. M. Anlage, A. Amar, and F. C. Wellstood, "Near-field scanning microwave microscope with 100 μm resolution," *Appl. Phys. Lett.*, vol. 69, pp. 3272–3274, Nov. 1996.

[11] S. Hunsche, M. Koch, I. Brener, and M. C. Nuss, "THz imaging in the near-field," in *CLEO'97 Tech. Dig.*, pp. 64–65.

[12] M. Tabib-Azar, N. S. Shoemaker, and S. Harris, "Non-destructive characterization of materials by evanescent microwaves," *Meas. Sci. Technol.*, vol. 4, pp. 583–590, 1993.

[13] S. Kawata, H. Takaoka, and Y. Inoue, "Slit-aperture SNOM for infrared spectroscopic micro-analysis," in *Near Field Opt. Conf. Dig.*, vol. 8, 1995, pp. 159–160.

[14] M. Golosovsky, A. Galkin, and D. Davidov, "High-spatial resolution resistivity mapping of large-area YBCO films by a near-field millimeter-wave microscope," *IEEE Trans. Microwave Theory Tech.*, vol. 44, pp. 1390–1392, July 1996.

[15] A. C. Kak and M. Slaney, *Principles of Computerized Tomographic Imaging*. New York: IEEE Press, 1988.

[16] G. T. Herman, Ed., *Image Reconstruction from Projections: Implementations and Applications, Topics in Applied Physics*. Berlin, Germany: Springer-Verlag, 1979, vol. 32.

[17] G. T. Herman, *Image Reconstruction from Projections: The Fundamentals of Computerized Tomography*. New York: Academic, 1979.

[18] M. A. Paesler and P. J. Moyer, *Near-Field Optics: Theory, Instrumentation and Applications*. New York: Wiley, 1996.

[19] A. Rosenfeld and A. C. Kak, *Digital Picture Processing*. New York: Academic, 1976.

[20] G. A. Massey, "Microscopy and pattern generation with scanned evanescent waves," *Appl. Opt.*, vol. 23, pp. 658–660, Mar. 1984.

[21] T. Nozokido, H. Minamide, J. Bae, T. Fujii, M. Itoh, and K. Mizuno, "Visualization of photoexcited free carriers with a scanning near-field millimeter-wave microscope," in *23rd Int. Infrared Millimeter Waves Conf. Dig.*, Colchester, U.K., Sept. 1998, pp. 382–384.

[22] T. Vogel, G. Dodel, E. Holzhauer, H. Saltzmann, and A. Theurer, "High-speed switching of far-infrared radiation by photoionization in a semiconductor," *Appl. Opt.*, vol. 31, pp. 329–337, Jan. 1992.

[23] T. Nozokido, H. Kudo, J. Bae, T. Saito, and K. Mizuno, "Improvements in resolution and image reconstruction for scanning near-field millimeter-wave microscopy using a metal slit-type probe," in *5th Int. Near-Field Opt. Related Tech. Conf. Dig.*, Shirahama, Japan, Dec. 1998, pp. 173–174.

[24] T. Nozokido, H. Kudo, J. Bae, and K. Mizuno, "Improvement in image reconstruction for scanning near-field millimeter-wave microscopy using a metal slit-type probe," unpublished.

Tatsuo Nozokido (M'99) received the B.Eng., M.Eng., and D.Eng. degrees in electrical engineering form Tohoku University, Sendai, Japan, in 1985, 1987, 1999, respectively.

From 1987 to 1991, he was a Researcher at the Central Research Laboratory, Hitachi Ltd., Tokyo, Japan. From 1991 to 1999, he was a Researcher at the Photodynamics Research Center, Institute of Physical and Chemical Research (RIKEN), Sendai, Japan. From 1999 to 2000, he was with the Rutherford Appleton Laboratory (RAL), Oxfordshire, U.K. He is currently an Associate Professor at the Research Institute of Electrical Communication, Tohoku University, Sendai, Japan. His current research interests include millimeter and submillimeter-wave sources and imaging systems.

Dr. Nozokido is a member of the Institute of Electronics, Information and Communication Engineers (IEICE), Japan, and the Japan Society of Applied Physics.

Jongsuck Bae (A'94–M'94–SM'98) was born in Nagoya, Japan, in 1953. He received the B.Eng. degree in electric engineering from the Korean University, Tokyo, Japan, in 1976, and the D.Eng. degree in electronic engineering from Tohoku University, Sendai, Japan, in 1990.

In 1977, he joined the Research Institute of Electrical Communication, Tohoku University, where he has been an Associate Professor since 1992. His research has been in developing quasi-optical components, such as oscillators, modulators, and couplers used for millimeter and submillimeter wavelengths, and their applications.

Dr. Bae is a member of the Institute of Electronics, Information and Communication Engineers (IEICE), Japan, and the Japan Society of Applied Physics.

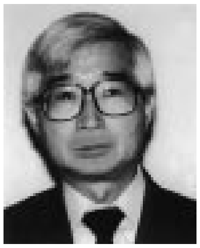

Koji Mizuno (M'72–SM'72–F'93) was born in Sapporo, Japan, on July 17, 1940. He received the B.Eng., M. Eng., and D. Eng. degrees in electronic engineering from Tohoku University, Sendai, Japan, in 1963, 1965, and 1968, respectively.

In 1968, he joined the Department of Electronic Engineering, Faculty of Engineering, Tohoku University, was appointed an Associate Professor at the Research Institute of Electrical Communication in 1972, and since 1984, has been a Professor of electron devices. In 1973, he spent a one-year sabbatical leave at Queen Mary College, University of London, London, U.K. and, in 1990, spent a six-month sabbatical leave at the California Institute of Technology, Pasadena, and Queen Mary and Westfield College, London, U.K. From 1990 to 1998, he was a Team Leader of the Photodynamics Research Center, Institute of Physical and Chemical Research (RIKEN), Sendai, Japan, where he ran a laboratory for submillimeter-wave research, as well as a laboratory at Tohoku University. He has been interested in the millimeter and submillimeter-wave region of the electromagnetic-wave spectrum, and his current work is in detection, generation, and their applications in the region.

Dr. Mizuno is member of the Institute of Electronics, Information and Communication Engineers (IEICE), Japan, the Institute of Electrical Engineers of Japan, and the Japan Society of Applied Physics. He was the recipient of the 17th Kagaku Keisoku Shinkokai (Scientific Measurement) Award in 1984 and the Kenneth J. Button Prize in 1998 for development of millimeter and submillimeter-wave devices.